Haptic Perception of Liquids Enclosed in Containers

Carolyn Chen

Electrical Engineering and Computer Sciences
University of California at Berkeley

Technical Report No. UCB/EECS-2019-140
http://www2.eecs.berkeley.edu/Pubs/TechRpts/2019/EECS-2019-140.html

October 25, 2019

Acknowledgement

This research was performed at the HARTLab at UC Berkeley in affiliation with the Berkeley AI Research (BAIR) Lab. The author was supported by the NSF-Graduate Research Fel-lowship. This work was originally published at the 2019 IEEE/RSJ International Conference on Intelligent Robots and Systems (IROS) in Macau with co-authors Robert Matthew and Ruzena Bajcsy. We thank our colleagues who provided helpful feedback and suggestions, in particular, Matthew Matl, Andrea Bajcsy, Somil Bansal, and Sarah Seko. The author is deeply grateful for the insightful feedback of her readers, Professor Ruzena Bajcsy and Professor Hannah Stuart.

Haptic Perception of Liquids Enclosed in Containers

by

Carolyn Matl (Chen)

A dissertation submitted in partial satisfaction of the

requirements for the degree of

in

Electrical Engineering and Computer Science

in the

Graduate Division

of the

University of California, Berkeley

Committee in charge:

Professor Ruzena Bajcsy, Chair
Professor Hannah Stuart

Fall 2019

Submitted to the Department of Electrical Engineering and Computer Sciences, University of California at Berkeley, in partial satisfaction of the requirements for the degree of **Master of Science, Plan II**. The project report of Carolyn Matl (Chen), titled Haptic Perception of Liquids Enclosed in Containers, is approved:

Chair ______________________ Date 10/14/2019

______________________ Date 10/25/2019

University of California, Berkeley

Haptic Perception of Liquids Enclosed in Containers

Abstract

Haptic Perception of Liquids Enclosed in Containers

by

Carolyn Matl (Chen)

in Electrical Engineering and Computer Science

University of California, Berkeley

Professor Ruzena Bajcsy, Chair

Service robots will require several important manipulation skills, including the ability to accurately measure and pour liquids. Prior work on robotic liquid pouring has primarily focused on visual techniques for sensing liquids, but these techniques fall short when liquids are obscured by opaque or closed containers. This paper proposes a complementary method for liquid perception via haptic sensing. The robot moves a container through a series of tilting motions and observes the wrenches induced at the manipulator's wrist by the liquid's shifting center of mass. That data is then analyzed with a physics-based model to estimate the liquid's mass and volume. In experiments, this method achieves error margins of less than 1g and 2mL for an unknown liquid in a 600mL cylindrical container. The model can also predict the viscosity of fluids, which can be used for classifying water, oil, and honey with an accuracy of 98%. The estimated volume is used to precisely pour 100mL of water with less than 4% average error. This work will be presented and published through the 2019 IEEE/RSJ International Conference on Intelligent Robots and Systems (IROS) in Macau.

To my parents, for always believing in me...
and my family and friends, for caring for me...
and my academic mom, Ruzena, for rooting for me...
and most of all to my husband and best friend, Matthew, for everything.

Contents

List of Figures

Acknowledgments

This research was performed at the HARTLab at UC Berkeley in affiliation with the Berkeley AI Research (BAIR) Lab. The author was supported by the NSF-Graduate Research Fellowship. This work was originally published at the 2019 IEEE/RSJ International Conference on Intelligent Robots and Systems (IROS) in Macau with co-authors Robert Matthew and Ruzena Bajcsy. We thank our colleagues who provided helpful feedback and suggestions, in particular, Matthew Matl, Andrea Bajcsy, Somil Bansal, and Sarah Seko. The author is deeply grateful for the insightful feedback of her readers, Professor Ruzena Bajcsy and Professor Hannah Stuart.

Chapter 1

Introduction and Related Work

1.1 Introduction

Perception of liquids inside closed containers has been studied for quite some time by the transportation and aerospace industries, where estimating the volume [18] or sloshing [10] of fuel inside a tank can be used to better control trucks or aircraft. With the advent of service robots that can work in the kitchen, this same problem has now resurfaced at a much smaller scale. *How much milk is inside the carton? How thick is the honey inside the jar?* Answering these questions before opening a container can drastically change how a robot might plan to pour a liquid [19, 9, 17, 34].

However, the complexity of fluid mechanics makes it difficult to accurately model and predict the behavior of liquids, and transparent liquids present a challenge for visual sensors. Several vision-based techniques have addressed this challenge [35, 31, 16], but these methods either only perceive the liquid during the pouring action or do not work when the container is opaque or occluded.

To address these challenges, this paper proposes a haptic-based method to complement existing visual techniques. Our robot rotates a container filled with an unknown liquid to shift the liquid's center of mass and observes the wrenches induced at the manipulator's wrist during both static and dynamic states of the liquid. The method then analyzes this wrench data with a physics-based model to estimate the liquid's mass, volume, and viscosity. To the best of our knowledge, this is the first paper to use robotic haptic sensing and physics-based reasoning to completely determine these three key parameters of liquids inside containers.

The main contributions of this paper are:

- Time-domain system identification of key parameters of liquids inside containers (mass, volume, and viscosity) using haptic data.
- A physics-based model that utilizes both the static and dynamic states of the liquid for parameter estimation.
- A demonstration of the use of liquid parameter estimation for robotic precision pouring.

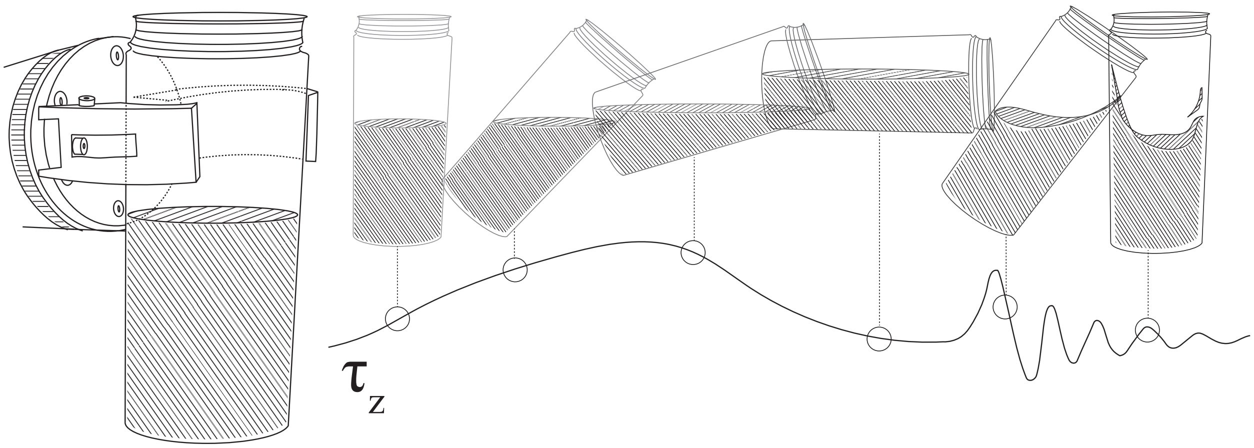

Figure 1.1: Wrench signals at the wrist of a robotic manipulator reflect changes in the center of mass of liquid inside a container. These signals are used to infer key properties of the liquid such as its mass, volume, and viscosity. Rotations are applied to the container in order to observe both static and dynamic behavior of the liquid.

1.2 Related Work

Liquid modeling and simulation

The high-dimensional and stochastic nature of fluid flow makes modeling and simulating liquids a challenging and often computationally-demanding task. By narrowing the scope to fluids in a container, it has been shown that basic equivalent mechanical models such as pendulums [8] or multi-mass-spring systems [28] can be sufficiently descriptive for certain objectives. Other work has explored numerical techniques such as the Volume of Fluid method combined with the Navier-Stokes equations to model liquid sloshing [36, 6] or particle-based simulations for tracking liquid flow [24, 35, 32]. A recognized strength of physics-based simulations is their ability to generalize to different liquids, as only few physical parameters such as viscosity need to be changed without the need to relearn a representative model [32]. However, the authors of [32] note that it is still an open challenge to efficiently observe such parameters from real data, which this paper aims to address.

Active perception and system identification

Inferring model parameters from sensor data is a fundamental focus in the fields of active perception [2] and system identification [1]. The majority of existing literature concerned with estimating liquid properties such as volume or viscosity tackles this challenge by using either special-purpose equipment such as multi-sensor fusion systems built in and around aircraft fuel tanks [18, 12] or camera-based systems that require advanced vision techniques and processing [7, 9]. This paper proposes a method for finding these parameters by using physics-based models on haptic data.

Interactive haptic perception of objects with internal dynamics

Liquids inside containers are part of the broad category of objects with internal dynamics. It has been shown that for objects in this class, such as articulated objects, [15, 14], direct interactions can allow robots to exploit the object's kinematics and dynamics to improve model information. These interactions can range anywhere from near-static contacts [11] to persistent excitation [3] to derived motions optimized for information gain [30]. In particular, pairing these interactions with haptic sensing enables perception of objects that are unobservable with vision (e.g., liquids in an opaque bottle). In [11, 4], the authors use tactile data during a grasp of a container to distinguish between an empty or full container. A more dynamic motion is applied in [3], in which shaking-induced vibrations are used to classify between different container contents. The angle and frequency of shaking is algorithmically determined to maximize information gain and to infer the viscosity of a liquid inside a container in [30]. While [30] addresses the generation of an action in order to best perceive viscosity, this paper uses predetermined motions informed by exploratory analysis with a greater focus on parameter estimation.

Manipulation of liquids

Accurate liquid modeling, simulation, and perception is essential for the manipulation of liquids. Slosh-control and pouring are two challenging robotic tasks within the realm of liquid manipulation. Control of tanks or containers while minimizing slosh has applications for ground vehicles, aerospace vehicles, and robotics [10, 28]. Instead of focusing on the control of slosh, the methods in this paper utilize slosh dynamics to determine the viscosity of a liquid. Numerous papers have also worked on the task of pouring liquids [35, 31, 33, 26, 27, 25, 16], although most rely on vision-based sensing to track liquid flow. Four works of note [29, 33, 16, 21] perform precision pouring, i.e., pouring of specific amounts of fluid. This paper also attempts this challenging task, but our method differs in that the haptic signals and physics-based reasoning inform the action to take *before* the liquid is poured.

Chapter 2

Problem Statement

Imagine a robotic manipulator that has a stable grasp of an opaque bottle encasing some amount of an unknown liquid. The manipulator is allowed to perturb the bottle in order to haptically perceive the internal dynamics of its contents. Given the wrench forces experienced at the wrist of the manipulator, the goal of this paper is to determine the mass, volume, and viscosity of the liquid enclosed in the container.

2.1 Simplifying Assumptions

It is assumed that the manipulator has already achieved a rigid grasp of the container, maintaining force closure throughout the entire interaction and perception cycle. We limit manipulator motions to rotations of the end-effector wrist joint, and to simplify processing, wrench forces are only measured when the manipulator is not in motion. With these assumptions, wrench forces at the wrist should primarily reflect the shifting center of mass of the liquid. By observing this proxy for aggregate motion of the liquid, the physics models proposed approach the problem macroscopically rather than at the molecular scale. The liquid is assumed to have uniform density and be at room temperature.

Concerning the container, many assumptions were made including that it is rigid and has a known mass and geometry. For much of the analysis in this paper, we use a cylindrical container and approximate its geometry with a right circular cylinder parameterized by its radius and length. While this geometric assumption enables fast analytic calculations, we can still perform the same analysis on arbitrarily-shaped containers using mesh processing techniques. Knowledge of the grasp point of the container, parameterized by the distance from the bottom of the container to the center of the grasp, is also assumed. Container wall thickness is assumed to be negligible so that the internal volume of the container can be determined from its external geometry, which we acknowledge will induce some small error in our analysis.

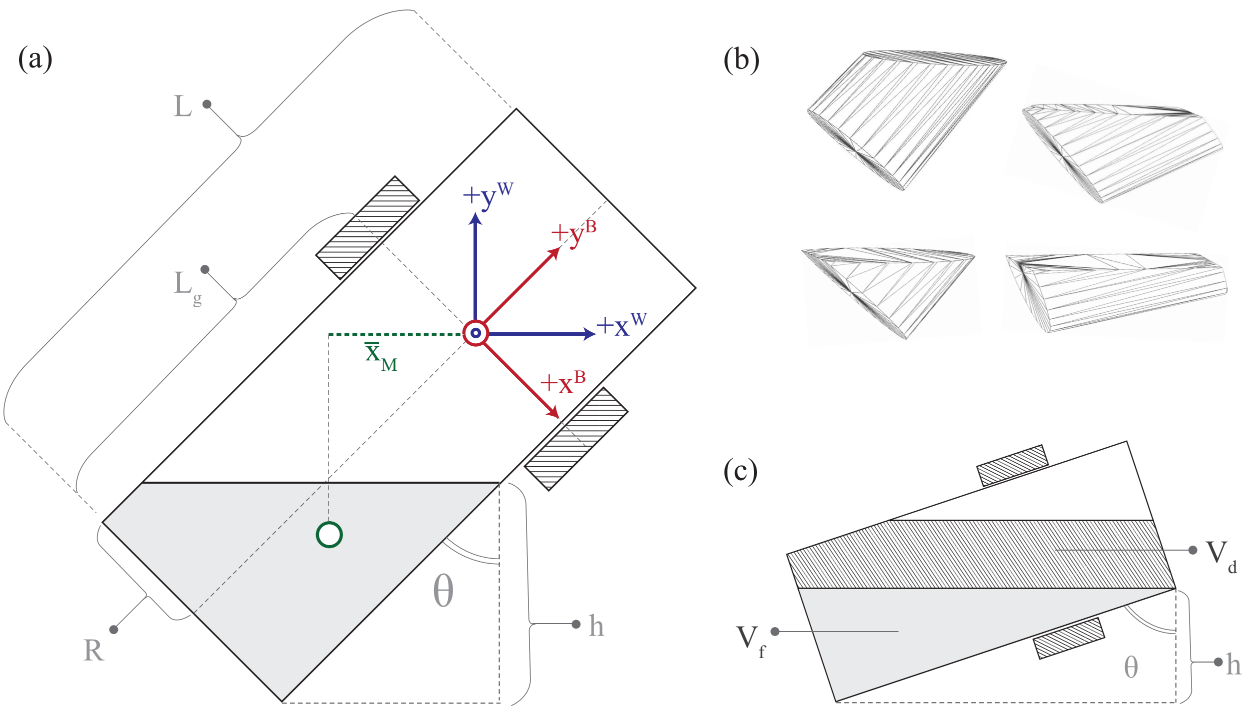

Figure 2.1: (a) A cross-sectional diagram defining variables used to derive parameter estimation formulas. (b) Top to bottom, left to right are the four cases of liquid geometry in a cylindrical container, visualized by the mesh approximation method. (c) A diagram to determine θ for a precise pour.

2.2 Definitions

Let the state of the system at time t be defined as $x_t = (f_t, \tau_t, \theta_t)$, where $f \in \mathbb{R}^3$ and $\tau \in \mathbb{R}^3$ are the forces and torques along the x, y, an z axes experienced at the wrist of the manipulator and $\theta \in [0, 2\pi]$ is the clockwise angle of rotation of the manipulator about the z-axis from the vertical. Based on this single-axis rotation constraint, the states of interest for the following experiments are f_x, f_y, and τ_z.

For a cylindrical container, let radius R and length L define its geometry. The robot grasp can be anywhere along the length of the container, and the position of the gripper center relative to the bottom face of the container is defined by the distance L_g. The wrench $F^B = (f^B, \tau^B)$ is originally with respect to the body frame of the system, which we define as rigidly attached to the center of the grasp with positive y pointing towards the top face of the container. The world frame is defined for $+y$ opposite of gravitational force, also with its origin centered between the grasp (see Figure 2.1).

The unknown values we wish to estimate are the mass m_ℓ, volume V, and the dynamic viscosity μ of the liquid. The total mass of the system is $M = m_g + m_c + m_\ell$, where m_g is the known mass of the gripper and m_c is the known mass of the container. Other unknown variables that are useful for calculations in the following section are the height of the liquid inside the container, h, and the center of mass of the composite system $\bar{x}_M = \bar{x}_g + \bar{x}_c + \bar{x}_\ell$, both of which are defined with respect to the world frame. We use $\bar{x}$ to represent the *horizontal* component of the center of mass. h is defined as the vertical distance from the lowest point of the container to the surface of the liquid. $\bar{x}_g$ is assumed to be 0 since it coincides with the origin of the world frame and $\bar{x}_c$ is assumed to be at the midpoint of the container. $\bar{x}_\ell$ is initially unknown. Figure 2.1 summarizes these definitions in a cross-sectional diagram of the system.

2.3 Objective

This paper aims to solve for m_ℓ, V, and μ given x_t for $t \in [t_0, t_1]$. A predetermined action is taken by the robot, involving a rotation of θ at some velocity $\dot{\theta}$. To simplify analysis, t_0 is defined as the time once this action is completed, and t_1 is a constant time after t_0 (in these experiments, 10 sec). The methods described in the following section are later evaluated by comparing m_ℓ, V, and μ to ground-truth values.

Chapter 3

Methods

Both static and dynamic signals are used to calculate m_ℓ, V, and μ given inputs f_x, f_y, and τ_z. The changing center of mass of the liquid, $\bar{x}_\ell$, is the key to deriving these values. For the following sections, assume the inputs are expressed with respect to the static world frame (see Figure 2.1).

3.1 Liquid Mass

Knowing m_c, the mass of the container, finding the mass of the liquid is simple. Given the force in the positive y direction, f_y, of the static world frame, then

$$m_\ell = {}^{f_y}\!/_{g} - m_g - m_c$$

where g is the gravitational constant $-9.807\,{}^{m}\!/_{s^2}$ and m_g is the measured mass of the gripper in kg.

3.2 Liquid Volume

Given the liquid mass from Section 3.1, we can derive an expression for the torque τ_z as a function of the control variable θ and the volume V, an unknown. First, we rewrite τ_z in terms of the centers of mass of the attached system:

$$\tau_z = f_y \bar{x}_M = g(m_g \bar{x}_g + m_c \bar{x}_c + m_\ell \bar{x}_\ell)$$

Because the world frame is anchored at the center of the gripper, let $\bar{x}_g = 0$. We can approximate $\bar{x}_c$ by assuming the container has a shell with a uniform density. Then, relative to the world frame, $\bar{x}_c = ({}^{L}\!/_{2} - L_g)\sin\theta$. Finally, observe that liquid takes the shape of its container, so $\bar{x}_\ell$ is a function of rotation angle θ, volume V, and container geometry. Together, we get an expression of τ_z as a function of θ and V:

$$\tau_z(\theta) = g(m_c({}^{L}\!/_{2} - L_g)\sin\theta + m_\ell \bar{x}_\ell(\theta, V)) \tag{3.1}$$

Let θ represent a vector of rotation angles from a sampled discrete set Θ. This expression allows us to perform nonlinear least squares (NLS) to estimate the parameter V. The objective is to minimize the residuals between our measured values $\tau_z(\theta)$ and our model-based estimated values:

$$V = \arg\min_V \|\tau_z(\theta) - g(m_c(L/2 - L_g)\sin\theta + m_\ell \bar{x}_\ell(\theta, V))\|_2^2 \tag{3.2}$$

Below, we describe two different methods that can be used to define the nonlinear function $\bar{x}_\ell(\theta, V)$.

Analytic Model

Many containers can be approximated with simplified geometry (e.g. a rectangular prism or a cylinder). For such containers, we can derive a closed-form analytic expression for $\bar{x}_\ell(\theta, V)$. Here, we define the derived equations for a circular cylinder with radius R and length L and express $\bar{x}_\ell^B$ and $\bar{y}_\ell^B$ with respect to the *body frame*, shifted along the $+y^B$ by L_g. In other words, the origin of the frame of reference lies at the center of the bottom face of the container, with $+x^B$ extending along the radius and $+y^B$ extending along the length of the container.

To make these calculations easier, we first compute the height of the liquid h in the container (see Section 2.2) as a function of V and θ. Because this function is not easily invertible, in practice we use the fact that $h(\theta, V)$ is a monotonically-increasing function in V and find the correct value of h via binary search.

We assume the liquid is at rest, with its surface parallel to the ground plane. Depending on h, R, L, and θ, the liquid takes on one of four cylindrical wedge shapes (See Figure 2.1 as illustration). Below, the four cases defining $\bar{x}_\ell(\theta, V)$ collectively form a piecewise continuous function. All formulas are defined for the range $\theta \in [0, \frac{\pi}{2}]$, but through reasoning about symmetry, the full range can be derived.

1. The bottom face is covered, but the top face is dry: This case occurs when $2R\sin\theta < L\cos\theta$ and $h \in [2R\sin\theta, L\cos\theta]$. Then:

$$\begin{aligned}
V &= \pi R^2(\frac{h}{\cos\theta}) - 2R\tan\theta) + \pi R^3 \tan\theta \\
\bar{x}_\ell^B &= \frac{\pi R^4}{4V}\tan\theta \\
\bar{y}_\ell^B &= \frac{1}{V}((R\tan\theta \\
&\quad + \frac{h}{\cos\theta} - 2R\tan\theta)^2(\frac{1}{2}\pi R^2) + (\tan^2\theta)(\frac{1}{8}\pi R^4))
\end{aligned}$$

2. The bottom face is partially covered and the top face is dry: This case occurs when $h \in [0, a]$ for $a = \min[L\cos\theta, 2R\sin\theta]$. We define the following variables to simplify our expression. Let $\alpha = R - \frac{h}{\sin\theta}$ and $\beta = \sqrt{R^2 - \alpha^2}$. Then:

$$
\begin{aligned}
V &= \tan\theta(\frac{2\beta^3}{3} - \alpha(\frac{\pi R^2}{2} - \alpha\beta - R^2 \arctan\frac{\alpha}{\beta})) \\
\bar{x}_\ell^B &= \frac{1}{V}\tan\theta(\frac{1}{4}(\frac{\pi R^4}{2} - \alpha\beta(2\alpha^2 - R^2) \\
&\quad - R^4 \arctan(\frac{\alpha}{\beta})) - \frac{2\alpha\beta^3}{3}) \\
\bar{y}_\ell^B &= \frac{\tan^2\theta}{V}(\frac{\alpha^2}{2}(\frac{\pi R^2}{2} - \alpha\beta - R^2\arctan\frac{\alpha}{\beta}) \\
&\quad + \frac{1}{8}(\frac{\pi R^4}{2} - \alpha\beta(2\alpha^2 - R^2) - R^4\arctan(\frac{\alpha}{\beta})) - \frac{2\alpha\beta^3}{3})
\end{aligned}
$$

3. The bottom face is covered and the top face is partially covered: This case occurs when $h \in [a, \cos\theta(L + 2R\tan\theta)]$ for $a = \max[L\cos\theta, 2R\sin\theta]$. The resulting cylindrical wedge is simply a volumetric difference of case (1) and (2). To be precise, let $V_i(\cdot)$, ${\bar{x}_\ell^B}_i(\cdot)$, and ${\bar{y}_\ell^B}_i(\cdot)$ represent the volume and center of mass formulas for case (i) as functions of height $(\cdot)$, with θ implied. Let $h_1 = h$ and $h_2 = h - L\cos\theta$. Then:

$$
\begin{aligned}
V_3 &= V_1(h_1) - V_2(h_2) \\
{\bar{x}_\ell^B}_3 &= \frac{{\bar{x}_\ell^B}_1(h_1)V_1(h_1) - {\bar{x}_\ell^B}_2(h_2)V_2(h_2)}{V_1(h_1) - V_2(h_2)} \\
{\bar{y}_\ell^B}_3 &= \frac{{\bar{y}_\ell^B}_1(h_1)V_1(h_1) - ({\bar{y}_\ell^B}_2(h_2) + L)V_2(h_2)}{V_1(h_1) - V_2(h_2)}
\end{aligned}
$$

4. The bottom and top faces are both partially covered: This case occurs when $L\cos\theta < 2R\sin\theta$ and $h \in [L\cos\theta, 2R\sin\theta]$. The resulting cylindrical wedge is a volumetric difference of two wedges of case (2):

$$
\begin{aligned}
V_4 &= V_2(h_1) - V_2(h_2) \\
{\bar{x}_\ell^B}_4 &= \frac{{\bar{x}_\ell^B}_2(h_1)V_2(h_1) - {\bar{x}_\ell^B}_2(h_2)V_2(h_2)}{V_2(h_1) - V_2(h_2)} \\
{\bar{y}_\ell^B}_4 &= \frac{{\bar{y}_\ell^B}_2(h_1)V_2(h_1) - ({\bar{y}_\ell^B}_2(h_2) + L)V_2(h_2)}{V_2(h_1) - V_2(h_2)}
\end{aligned}
$$

As shown, there is not a clean formulation for an expression that maps V to h. Instead, because $V(\cdot)$ is a monotonically increasing function with respect to the variable h, h can be found via binary search for the volume V. After this computation, $\bar{x}_\ell^B$ and $\bar{y}_\ell^B$ are transformed into the world frame.

Mesh Approximation

When a container has more complicated features such as in Figure 4.1, solving for closed-form expressions for volume and center of mass becomes much more challenging. For such containers, we provide an alternative method using polyhedral mass property calculations on mesh approximations [5, 23].

Similar to the method used in [33] and described in [37], we can bisect the container's mesh with a horizontal plane at different heights h and solidify the part of the mesh in the lower halfspace to approximate the shape of the liquid in the container at height h. As in the analytic method, we compute h for a given V by using binary search. The center of mass of the resulting solid is computed using methods described in [23] and implemented in [5]. The analytic and computational mesh methods were verified to produce the same approximate values.

3.3 Liquid Viscosity

In contrast with prior sections, viscosity calculations exploit the dynamic modes of the liquid. In particular, we aim to induce either sloshing within the container or laminar flow down its side. For low-viscosity fluids like water, viscosity can be determined by observing the decaying oscillations of the forces caused by the sloshing. For highly-viscous fluids such as honey, the damped response of the forces can be used to approximate viscous fluid flow.

Slosh-induced forces and torques are caused by the shifting center of mass of the liquid inside the container. The slosh mode that dominates the force profile is the fundamental antisymmetric wave, which is characterized by a slosh wave peaking at one end of the container and sinking at the other [8]. In a stationary tank, slosh oscillation decays reflect energy dissipation due to viscous stresses within and at the boundary of the liquid [8]. Several works studying sloshing in a tank have empirically shown that the decay rate of the oscillations is solely a function of tank geometry, fill level, and liquid viscosity. Specifically, [8, 22, 13] define the following. Let $\Delta = \frac{\text{peak amplitude of oscillation}}{\text{peak amplitude of oscillation one cycle later}}$ be the logarithmic decrement of the decaying oscillation. The damping ratio is then defined by:

$$\gamma = \frac{\Delta}{\sqrt{2\pi^2 + \Delta^2}} \tag{3.3}$$

For an upright circular cylindrical tank, the damping ratio of the first symmetric mode is given by:

$$\gamma = 0.79\sqrt{\frac{\nu}{R^{3/2}g^{1/2}}}[1 + \frac{0.318}{\sinh 1.84h/R}(\frac{1-(h/R)}{\cosh 1.84h/R} + 1)] \tag{3.4}$$

where ν is the kinematic viscosity of the liquid, R is the radius of the tank, and h is the fill-level of the tank.

For a container with a different geometry, [13] provides a table of constants C_1 and n_1 corresponding to the characteristic dimension d and the following relation: $\gamma = C_1(\frac{\nu}{d^{3/2}\sqrt{g}})^{n_1}$

This paper thus aims to induce oscillations for cylindrical containers in the upright position. The input motion we chose is a single impulse rotation from $\theta = \pi/2$ to $\theta = 0$. With γ calculated using Equation 3.3 and h calculated using techniques described in Section 3.2, the viscosity can be calculated by rearranging Equation 3.4:

$$\nu = \gamma^2 \sqrt{R^3 g}[0.79(1 + \frac{0.318}{\sinh 1.84h/R}(\frac{1-(h/R)}{\cosh 1.84h/R} + 1))]^{-2} \tag{3.5}$$

To get the dynamic viscosity, μ, we multiply ν by the inferred density of the liquid ρ.

For highly-viscous fluids like honey, the response is over-damped, meaning no oscillations will occur in the wrench profile. For this case, we estimate the dynamic viscosity μ by approximating the flow once the container is tilted from $\theta = \pi/2$ to $\theta = 0$ as a free surface flow on an inclined plane. [20] defines the mass flux per unit length $\mathcal{Q}$ as

$$\mathcal{Q} = \frac{\rho g \cos\theta h_2^3}{2\mu} \tag{3.6}$$

where $\theta = 0$, ρ is the density of the liquid, and h_2 is the thickness of the liquid. We assume h_2 to equal the height of the liquid at steady state when the container is tilted horizontally ($\theta = \pi/2$). $\mathcal{Q}$ can be approximated by $\frac{\Delta m_\ell}{t_r A}$ where t_r is the 10 to 90% rise time of the damped torque response and $A = \frac{R^2}{2}(\alpha - \sin\alpha), \alpha = 2\arccos(\frac{R-h}{R})$ is the cross-sectional area of the liquid flow sliced parallel to the ground plane. Letting h be the steady state height of the liquid when the container is tilted at $\theta = 0$, we can approximate Δm_ℓ by the mass quantity estimated to move during fluid flow induced by the rotation, or $\Delta m_\ell = m_\ell(\frac{V-Ah}{V})$. Finally, rearranging Equation 3.6, we get:

$$\mu = \frac{\rho g \cos\theta h_2^3}{2\mathcal{Q}}$$

3.4 Pouring

Building on the concepts discussed above, we investigate a simple control scheme to pour a specific volume of liquid. Using estimation of the volume V, we can determine a rotation angle θ to pour a specified volume from the container.

Referencing Figure 2.1, let V be the starting volume, V_d be the desired poured volume, and $V_f(\cdot)$ be the final volume of the liquid in the container, corresponding to height $(\cdot)$. We assume that the liquid flow is laminar and that, at the optimal angle θ, V_d is the volume of the liquid above the horizontal plane intersecting the bottom-most point of the container's top face if the container were closed. The objective then is to solve for θ:

$$\theta = \underset{\theta\in[0,\pi/2]}{\arg\min} \|V_d - (V - V_f(L\cos\theta))\|_2^2 \tag{3.7}$$

Because V_f monotonically decreases as $\theta \to \pi/2$, a binary search is used to find θ. The pouring experiments only use cylindrical containers, but it is possible to pour from containers of more complicated geometry by using the mesh-approximation method described in section 3.2.

Chapter 4

Experimental Setup

4.1 Hardware system

All the experiments in this paper use a Universal Robot UR5 (5 kg payload) robotic arm. While the UR5 has 6 degrees of freedom, for simplicity, the experiments only rotate the 6th joint, or wrist 3, to move the container. An ATI Axia80 EtherNet Force/Torque (F/T) sensor is attached at the end-effector. The six-axis sensor has a 7812 Hz output frequency rate and coincides with the body frame depicted in Figure 2.1. Attached to the F/T sensor is a 3D-printed mechanically-adjusted parallel-jaw gripper. High durability grip tape in the inside of the gripper ensures minimal slippage.

Different types of liquids and cylindrical containers were tested during experimentation, illustrated in Figure 4.1. The different liquids were chosen to represent a range of viscous materials found in a typical kitchen. Different sized and massed cylindrical bottles were used to test their effect on parameter estimation.

4.2 Signal processing

The time-series F/T sensor data and UR5 joint data are recorded asynchronously. These are then aligned using system time stamps, down-sampled using a Finite Impulse Response filter, and interpolated so that the F/T and joint position sensors are sampled at the same point in time. F/T sensor offsets measured during a calibration phase are subtracted from the interpolated and down-sampled F/T data. Using the joint position data, a transformation is applied to the six-axis F/T data to convert the wrench from the body frame F^B to the static world frame F^W. Finally, a 1D Gaussian filter with $\sigma = 5$ is applied to all six axes to denoise the data.

Figure 4.1: From left to right: 48oz Nalgene water bottle used in exploratory analysis, 3 large cylindrical containers used in viscosity estimations, 3 small cylindrical containers used in all experiments, and isopropyl alcohol, coconut milk, canola oil, evaporated milk, mango juice, dish soap, syrup, and honey, arranged in order of approximately increasing viscosity.

4.3 Exploratory analysis

Prior to experimentation, we performed exploratory analysis on preliminary data. Our first exploration involved filling the $1.5L$ Nalgene with water to $375mL$ and $750mL$ and rotating it at 19 different angles evenly spaced by 10 deg, $\theta \in [0, 180]$ deg. Three different grasp locations were tested – at $L_g = {}^1\!/_4 L$, ${}^1\!/_2 L$, and ${}^3\!/_4 L$. The resulting data, depicted in Figure 4.2, demonstrates the repeatability of the F/T data and confirmed that τ_z alone was sufficiently informative to infer volume. The rest of the experiments use a grasp at $L_g = {}^3\!/_4 L$ in order to maintain greater stability during pouring. Furthermore, from Figure 4.2, it can be seen that this grasp position has a greater torque response for lower rotation angles, meaning less motion is necessary to extract approximately the same amount of information.

Finally, to ensure that Equation 3.2 could be optimized, we performed a grid search over the variable V. As shown in Figure 4.2, the objective appeared to be convex, so NLS should produce good estimates of the true solutions.

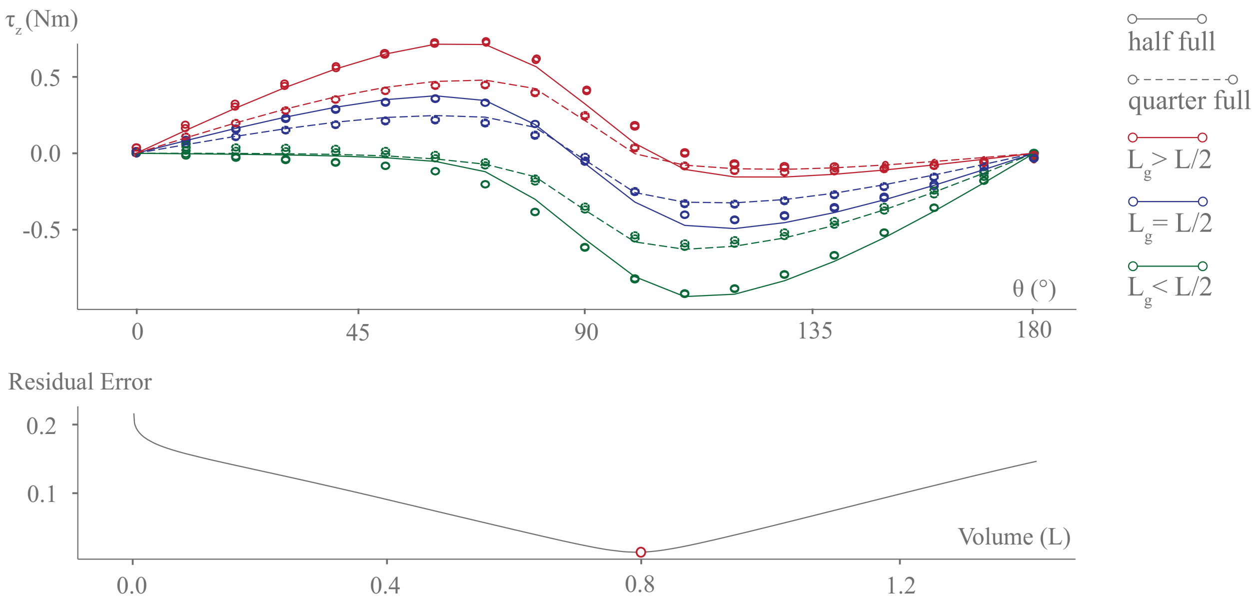

Figure 4.2: (top): Torques measured during a rotation of a half and quarter full Nalgene. Open points represent measured data, and lines represent the predicted torques, demonstrating that our model matches measurements well for different grasp positions and volumes. (bottom): Graph of the residual error between measurements and predictions over the variable V. The convexity of the residual informs us that there should be a global minimum solution.

Chapter 5

Results and Discussion

Predetermined actions are applied to various liquid/container combinations and the accuracy of mass, volume, and viscosity estimations are evaluated below. Note that the mass and volume can be calculated from the same motion. Both calculations assume the liquid is in a static state, so a slow rotation from 0 to 180 deg, stopping at intervals of 10 deg, is applied for these estimations. In contrast, the viscosity estimations rely on observing the dynamic modes of the liquids, so a fast rotation from 90 to 0 deg is applied. Finally, for precision pouring, the applied rotation is computed using the estimated volume. Please see the accompanying video for visualizations of the following experiments.

5.1 Liquid Mass Estimation

We begin with liquid mass estimation by conducting a sensitivity experiment with varying fill-levels of a container. The small cylindrical container depicted in Figure 4.1 is used, which has an external radius and length of 35 and 172 mm, respectively, with a total measured capacity of 662mL. We sampled 13 fill-levels of water, evenly spaced from 0 to 100 percent full, and measured the ground-truth mass. For each fill-level, we performed five iterations of rotating the container from $\theta = 0$ to 180 deg, stopping every 10 deg to let the liquid settle. f_y is calculated for each instance by averaging over the transformed f_y^Ws throughout the entire motion. As shown in grey in the top-left plot of Figure 5.1, there is a gradual increase in the error of our mass estimate as the fill-level increases. This error could be attributed to a miscalibrated conversion from strain-gauge measurements to forces. Because the error appears to grow linearly with an increased mass, we fit a linear regressor to "re-calibrate" measured f_y forces. In the same figure in blue, we see that this re-calibration helps center the error of the mass estimation at an average error of -0.23g with a 95% confidence interval of $\pm$0.73g.

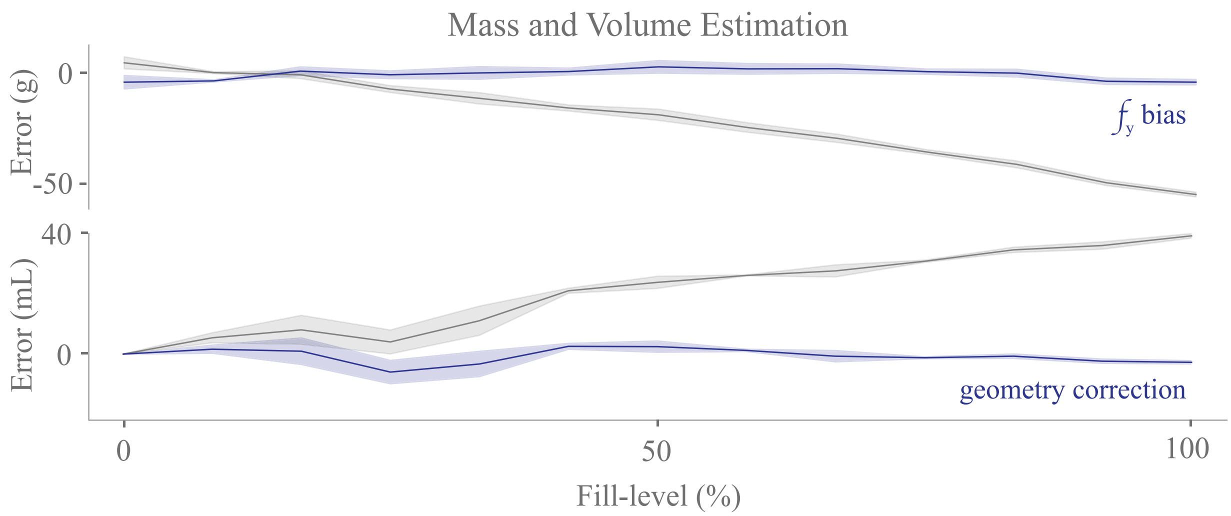

Figure 5.1: Error of mass and volume estimations. Blue curves represent adjustments of f_y measurements and corrections to reflect a better estimate of internal container geometry.

5.2 Liquid Volume Estimation

The same motion is used for liquid volume estimation. With the data from Section 5.1, we can observe the empirical error on our estimation of volume for different fill-levels of the small cylindrical container. The sampled measurements of τ_Z at different values of θ along with our estimate of m_l allow us to search for a volume V that minimizes the error between the measurements and our calculated τ_Z curve using Equation 3.1. Our first attempt resulted in a large average error, aggregated across all fill-levels, of 87 ± 53mL. However, a closer look revealed that this large error was due to the edge case of $m_l = 0$, for which the objective was not convex. Because we use the shifting center of mass to determine V, there is no way of discerning an empty container from a full container. Thus, our optimization consistently estimated $V = L\pi R^2$ when $\theta = 0$. However, knowledge of the container mass disambiguates the value of m_l, so we can bias the estimator to assume $V = 0$ if $m_l = 0$.

From Figure 5.1, we see that, with this bias, volume estimation performs with an error of 21.46 ± 3.28mL. Notice that our calculations tend to overestimate the actual liquid volume, as expected since we assume internal container geometry is equivalent to external geometry. If we reason about the geometry of the container's cavity, e.g., walls could be $1mm$ thick, then we see that this lowers the 95% confidence interval of the error to -0.65 ± 0.83mL. All 65 estimates of volume were within 13mL of error. Lower volume estimates tended to have greater variance, perhaps due to higher sensitivity to sensor noise. Note that while we tested mass and volume estimation on water, the physics-based calculations will work for any liquid as long as measurements are recorded when the liquid is in steady state.

Using NLS optimization allows for an efficient search of the volume estimate, but to verify that it indeed is finding the global minimum of the objective function, we evaluated the objective with a fine grid search over all possible volumes. Taking the global minimum solution found via grid search, the error in the volume estimate was essentially equivalent to that of using the more efficient NLS method, at a 95% confidence of -0.62 ± 0.82mL. The error-per-fill-level graph is visually identical to the one produced via NLS so it is omitted from Figure 5.1.

Finally, we tested liquid volume estimation using the mesh approximation method. A half-gallon milk carton (total capacity equivalent to about 1.9L) was measured and modeled as a 3D mesh. The milk carton was filled to 250mL, 500mL, and 750mL with water, and five iterations of tilts and measurements were performed per each fill level. Using the 3D mesh of the milk carton, the 95% confidence error margin of the volume estimation optimization was 1.69 ± 24.69mL.

5.3 Liquid Viscosity Estimation

We apply a different motion to the container here in order to observe the liquid in its dynamic mode. Instead of a slow rotation, we use a fast rotation from $\theta = 90$ to $0\,\text{deg}$ to act as an impulse to the system. The dynamics can be observed via both f_x^W and τ_z^W. If the resulting signals contain oscillations, the algorithm calculates μ via the slosh-dynamics analysis described in Section 3.3. Otherwise, the overdamped response is used to calculate μ via the fluid-flow equation (3.6). We tested this method of viscosity estimation on nine different liquids – water, oil, honey, isopropryl alcohol, coconut milk, evaporated milk, mango juice, dish soap, and syrup. Each liquid was poured into the small cylindrical container at 137, 292, and 442 mL and a series of five impulse rotations were applied in each scenario. To test the method's sensitivity to varying geometries, we also perform five impulse rotations to 636.11 mL of water, oil, and honey, each in a larger cylindrical container depicted in Figure 4.1.

As illustrated in Figure 5.2, while the variance of the viscosity estimates is high (note, however, on a log scale), the method manages to capture relative viscosity differences between the liquids. In fact, using the predicted viscosities of data from volumes of 292, 442, and 636 mL, a linear SVM classifier with 5-fold cross-validation is able to distinguish between the four lowest viscosity liquids at an accuracy of $78 \pm 11\%$ and between water, oil, and honey with an accuracy of $98 \pm 10\%$. These predictions improve if we narrow the training set to larger quantities of volume. This suggests that Equations 3.4 and 3.6 serve as reasonable parameterizations of the haptic signal τ_z. Furthermore, the method generalizes well to data captured using the larger container. For instance, estimates of the 636 mL of honey had an error of 0.197 ± 0.096 Pa·s when honey's true viscosity is approximately 10Pa·s.

The predominant limitations of the reported method that likely contributed to the wide variance in viscosity estimations are low signal-to-noise ratios (SNR)s of the haptic data as well as imperfect models. Many of the signals collected using the small container had low SNRs, often detecting one or two peaks before the signal was obscured by sensor noise. In contrast, with the larger container and quantity of liquid, the changes in the liquid center of mass were much clearer, as evidenced in signals shown in Figure 5.2. Subsequently, viscosity estimates made from larger containers tended to have a lower variance than those made based on observations with the smaller container. To combat this issue, a more dynamic-sensitive tactile or haptic sensor could be used, paired with an intelligent selection of shaking motions to improve SNR, similar to the active learning framework demonstrated in [30]. As expected, the models used to estimate viscosity were imperfect. For example, the clustering of the estimates of honey are illustrative of the sensitivity of the proposed model to changes in geometry and volume. A better model is needed to overcome these sensitivities.

5.4 An Application Demonstration: Pouring

To demonstrate the applicability of the methods described in this paper, we attempt to pour a specific amount of liquid given estimations of liquid volume. In contrast with other precision-pouring papers, this paper pre-computes an open-loop control strategy (specifically, the rotation angle θ) based on the estimated volume. While the proposed control scheme is not very sophisticated, it achieves reasonable effectiveness in this challenging task using only the haptically-estimated volume. Furthermore, this pre-computed rotation angle can act as a guide when paired with closed-loop control schemes, which can serve to dynamically fine-tune or adjust the angle.

We begin by characterizing the robot's pouring precision. Using Equation 3.7 and perfect knowledge of the liquid volume, we attempt to precisely pour a quarter, half, and three-quarters of 200, 400, and 500 mL of water from the small cylindrical container, with 5 trials for each case. At first, all attempted pours were approximately 50mL below the desired poured volume. After observing a few pours, it was evident that there were two factors contributing to this experimental error. The first is that there was a lip to the cylindrical container, where the radius of the open top was actually significantly smaller than the external radius. To fix this error, we assume that computer vision techniques can be used to estimate the internal radius, wall thickness, and lip dimensions of the container. This is a reasonable assumption as the lid would be off, exposing the true internal geometry of the container. The second factor contributing to error was the surface tension of the water. It was so strong that water would bunch up at almost 5mm above the bottom-most point of the lip, contributing to a significant difference between our model prediction and experimental results. To combat this, we added a term to represent the added height required due to water tension. With these changes, our robot became very precise and repeatable. Under perfect knowledge, the robot operates with an error of at most ± 5 mL poured, with an average error of 1.55 ± 1.60 mL.

We then attempted to precisely pour 100 mL from 200, 300, 400, and 500 mL of water based on the estimated volume of the water, with 5 trials for each case. Here, we make no assumption of the density of the liquid and only base our calculations off of estimates of V. As before, we found that the precision of pouring was incredibly sensitive to the a priori knowledge determining the container geometry. With knowledge of internal container geometry, the original volume estimated is more accurate (5.09±2.59mL) which subsequently allows for a more precise pour. For a 100 mL pour over 20 trials, the robot achieved an average error of 1.80 ± 2.04mL, where the largest error poured was +9mL. These results are comparable to related work that uses visual reasoning to precisely pour liquids. Finally, we attempted to pour oil and honey, but these both caused a giant mess and so we decided to postpone those experiments for the time being. However, a reasonable next step would be to incorporate estimated viscosity data for different liquids to guide the *speed* at which the pour is performed for minimal sloshing and maximal efficiency.

5.5 Discussion and Future Work

In this paper, we show that physics-based analysis of haptic signals can achieve high precision estimation of the mass and volume of liquids in a cylindrical container and provide a framework for estimating fluid viscosity. To demonstrate the efficacy of these methods, we performed precise pouring of water where the estimated volume determined the rotation angle θ. In future work, we plan to incorporate real-time haptic and visual control to improve precision during pouring. Furthermore, we hope to improve the precision of our viscosity estimates by combining better physics-based parameterization with active perception to optimize for motions to induce higher SNRs of the haptic data. More accurate viscosity measurements could then be used to inform a control strategy to quickly pour viscous fluids with minimal sloshing [34]. Finally, we would like to extend this work to haptic perception and control of granular materials and more non-newtonian fluids in containers.

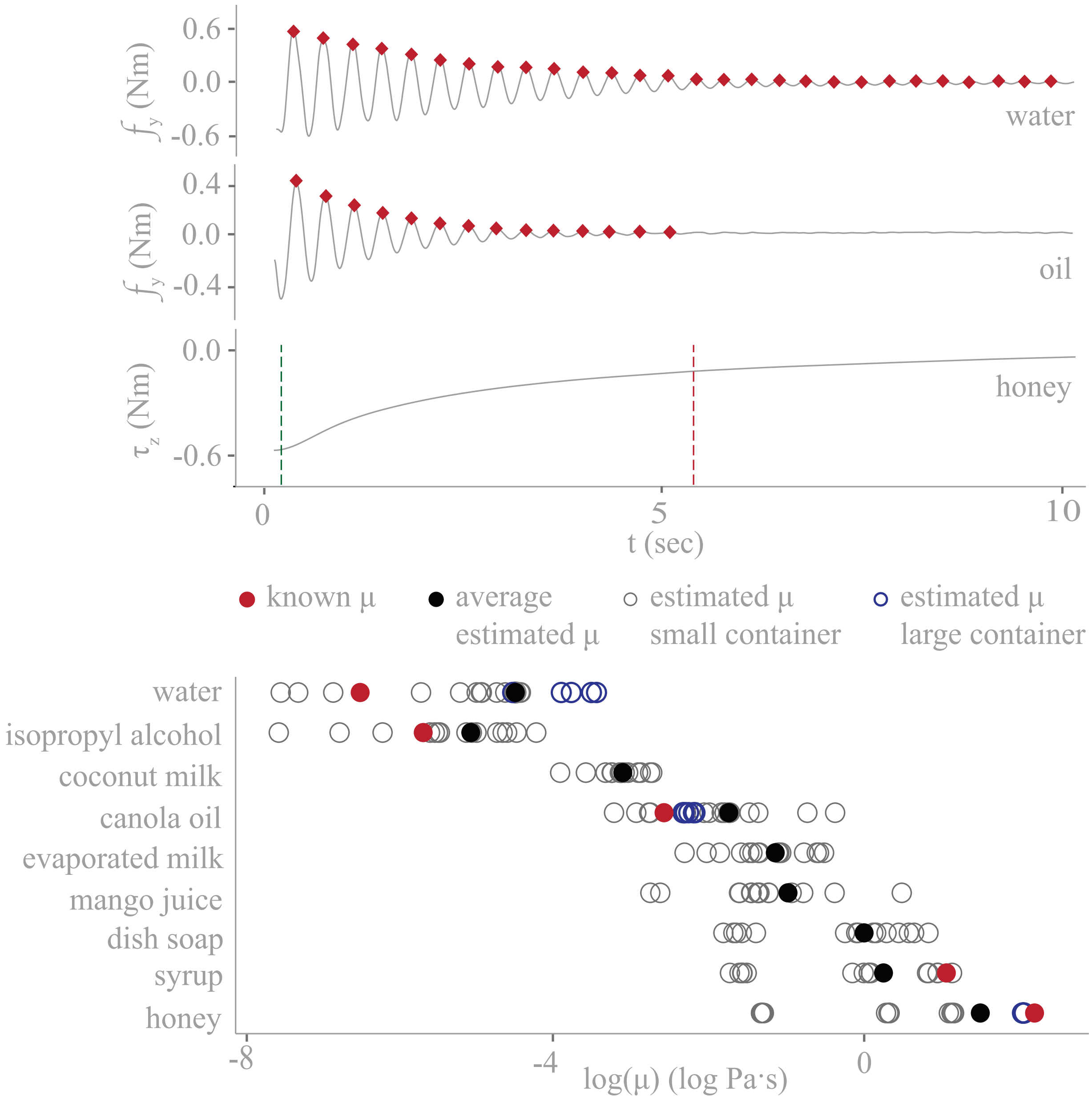

Figure 5.2: (top) Real f_y and τ_z data (filtered and smoothed) after a $90 \rightarrow 0$ deg rotation of water, oil, and honey in the large containers. Detected peaks and rise times used in viscosity calculations are shown. (bottom) Viscosity predictions for the 9 different liquids, arranged from top to bottom with increasing true viscosities. True values of five liquids are denoted by red. Black circles mark the averages of the estimated viscosities per liquid. Note, for illustrative purposes, viscosity estimates are shown on a log scale.

Appendix A

Derivations

A.1 Liquid Mass

Given the force oriented in the positive y direction, f_y, of the static world frame, which aligns with the negative of the gravitational force vector, then f_y is due to the collective mass of the end-effector attachment, i.e., the mass of the container m_c, the mass of the gripper m_g, and the mass of the contained liquid, m_ℓ. We want to find m_ℓ, and all other quantities are known, so:

$$\begin{aligned} f_y &= g(m_c + m_g + m_\ell) \\ {}^{f_y}/_{g} - m_g - m_c &= m_\ell \end{aligned}$$

A.2 Liquid Volume

Here, we derive the piecewise continuous equations that define the analytic model of liquid volume in a circular cylindrical container. First, we rewrite the torque τ_z about the wrist of the robot in terms of the centers of mass of the attached system (see Figure A.1):

$$\begin{aligned} \tau_z &= f_y \bar{x}_M \\ &= g(m_g + m_c + m_\ell)\frac{m_g \bar{x}_g + m_c \bar{x}_c + m_\ell \bar{x}_\ell}{m_g + m_c + m_\ell} \\ &= g(m_g \bar{x}_g + m_c \bar{x}_c + m_\ell \bar{x}_\ell) \end{aligned}$$

As depicted in Figure A.1, the world frame is anchored at the center of the gripper. Thus, $\bar{x}_g = 0$. Since we assume that the container has a shell with a uniform density, then relative to the world frame, $\bar{x}_c = ({}^{L}/_{2} - L_g)\sin\theta$. Note that $\bar{x}_\ell$ will be a function of the rotation angle θ, the volume V, and the container geometry. Thus, we get an expression of τ_z as a function of θ and V:

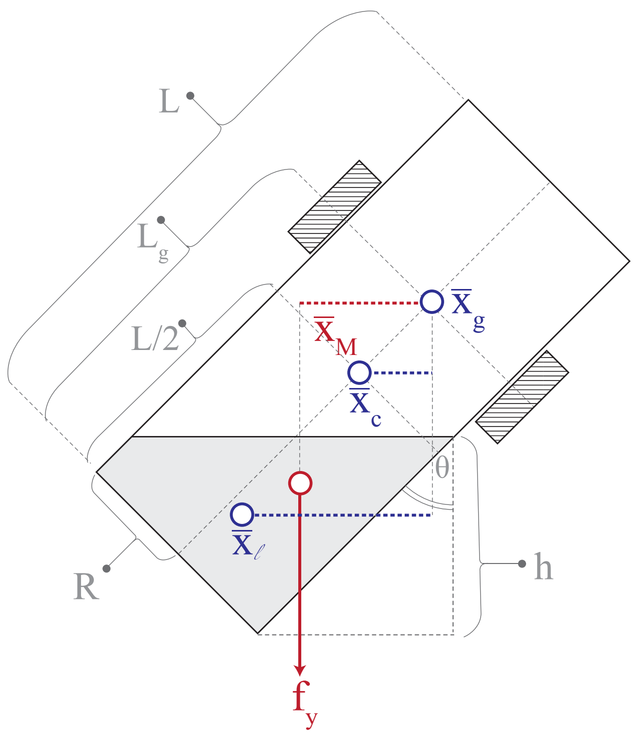

Figure A.1: A cross-sectional diagram defining variables used to derive liquid volume calculations. Example locations of center of masses of the container, gripper, and liquid are illustrated.

$$
\begin{aligned}
\tau_z(\theta) &= g(m_g * 0 + m_c * ((L/2 - L_g)\sin\theta) + m_\ell * \bar{x}_\ell(\theta, V)) \\
&= g(m_c((L/2 - L_g)\sin\theta) + m_\ell \bar{x}_\ell(\theta, V))
\end{aligned}
$$

Finding V becomes an optimization problem, where we want to minimize the residuals between the measured torques at different rotation angles $\tau_z(\theta)$ and our model-based estimated values:

$$V = \arg\min_V \|\tau_z(\theta) - g(m_c(L/2 - L_g)\sin\theta + m_\ell \bar{x}_\ell(\theta, V))\|_2^2$$

Below, we show full derivations of how we define the piecewise nonlinear function $\bar{x}_\ell(\theta, V)$. All calculations of $\bar{x}_\ell^{B*}$ and $\bar{y}_\ell^{B*}$ are made with respect to a shifted body frame $B*$, where the origin is centered at the bottom face of the cylindrical container (see Figure A.2). To transform the center of mass coordinates to world coordinates, the following transformation is applied:

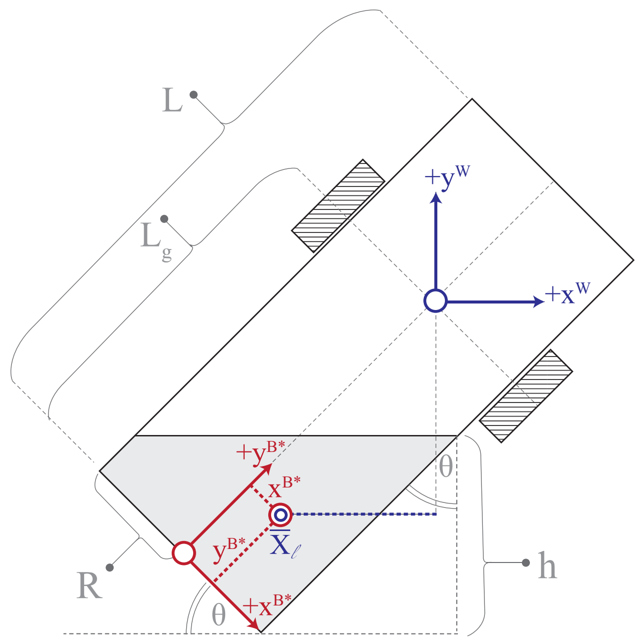

Figure A.2: An illustration of the shifted body frame $B*$, with respect to which the center of mass equations $\bar{x}_\ell^{B*}$ and $\bar{y}_\ell^{B*}$ are initially defined. $\bar{x}_\ell(\theta, V)$ is defined with respect to the world frame, so a transformation is necessary once $\bar{x}_\ell^{B*}$ and $\bar{y}_\ell^{B*}$ are computed.

$$\begin{bmatrix} \bar{x}_\ell^W \\ \bar{y}_\ell^W \\ 1 \end{bmatrix} = \begin{bmatrix} \cos -\theta & -\sin -\theta & L_g \sin(-\theta) \\ \sin -\theta & \cos -\theta & -L_g \cos -\theta \\ 0 & 0 & 1 \end{bmatrix} \begin{bmatrix} \bar{x}_\ell^{B*} \\ \bar{y}_\ell^{B*} \\ 1 \end{bmatrix}$$

and since we restrict the following definitions to $\theta \in [0, \frac{\pi}{2}]$ (symmetric reasoning leads to the derivation of the full range for theta), we can rewrite the transformation as:

$$\begin{bmatrix} \bar{x}_\ell^W \\ \bar{y}_\ell^W \\ 1 \end{bmatrix} = \begin{bmatrix} \cos\theta & \sin\theta & -L_g \sin\theta \\ -\sin\theta & \cos\theta & -L_g \cos\theta \\ 0 & 0 & 1 \end{bmatrix} \begin{bmatrix} \bar{x}_\ell^{B*} \\ \bar{y}_\ell^{B*} \\ 1 \end{bmatrix}$$

Thus, we can calculate the expression $\bar{x}_\ell(\theta, V)$ used in the optimization for V, which is equivalent to $\bar{x}_\ell^W$:

$$\bar{x}_\ell(\theta, V) = \bar{x}_\ell^{B*} \cos\theta + \bar{y}_\ell^{B*} \sin\theta - L_g \sin\theta$$

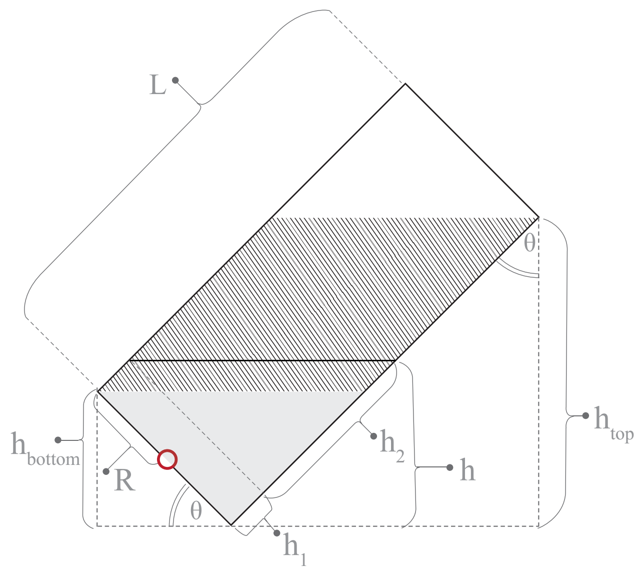

Figure A.3: Diagram depicting Case 1 for liquid center of mass and volume calculations.

Case 1: Bottom end covered, top end dry

Finding the bounds for h

This case occurs when $h_{top} > h_{bottom}$ and h is within the bounds h_{bottom} and h_{top}. Geometric reasoning finds that $h_{bottom} = 2R\sin\theta$ and $h_{top} = L\cos\theta$. Thus, we have the case condition that $L\cos\theta > 2R\sin\theta$ and $h \in [2R\sin\theta, L\cos\theta]$.

Finding the expression for V

A simple way to find the expression for V for this specific case is by breaking the liquid volume into two parts, corresponding to the two values h_1 and h_2, denoted in Figure A.3.

We first find h_2 with respect to known values R and θ:

$$\tan\theta = \frac{h_2}{2R}$$
$$2R\tan\theta = h_2$$

We can write h_1 in terms of h, R, and θ:

$$\begin{aligned}
\cos\theta &= \frac{h}{h_1 + h_2} \\
h_1\cos\theta + h_2\cos\theta &= h \\
h_1\cos\theta &= h - h_2\cos\theta \\
h_1 &= \frac{h}{\cos\theta} - h_2 \\
h_1 &= \frac{h}{\cos\theta} - 2R\tan\theta
\end{aligned}$$

Then the volumes corresponding to h_1 and h_2 are simply $\pi R^2 h_1$ and $\frac{1}{2}\pi R^2 h_2$. In terms of h, R, and θ, the combined volume can be expressed as such:

$$V = \pi R^2\left(\frac{h}{\cos\theta} - 2R\tan\theta\right) + \pi R^3\tan\theta$$

Finding expressions for the center of mass coordinates

Calculated with respect to a shifted body frame, with the origin centered at the red ring in Figure A.3, we solve the following integrals:

$$\begin{aligned}
\bar{x}_\ell^{B*} &= \frac{1}{M}\int\int\int x\rho dV = \frac{1}{M}\left(\frac{M}{V}\right)\int_{-R}^{R}\int_{-\sqrt{R^2-x^2}}^{\sqrt{R^2-x^2}}\int_{0}^{(R+x)\tan\theta+h_1} xdydzdx \\
&= \frac{1}{V}\left[\int_{-R}^{R}\int_{-\sqrt{R^2-x^2}}^{\sqrt{R^2-x^2}}(R+x)\tan\theta xdzdx + \int_{-R}^{R}\int_{-\sqrt{R^2-x^2}}^{\sqrt{R^2-x^2}} h_1 xdzdx\right] \\
&= \frac{1}{V}\left[2(R\tan\theta + h_1)\int_{-R}^{R} x\sqrt{R^2-x^2}dx + 2\tan\theta\int_{-R}^{R} x^2\sqrt{R^2-x^2}dx\right] \\
&= \frac{1}{V}\Bigg[2(R\tan\theta + h_1)\Big(-\frac{1}{3}(\cancel{R^2-x^2})^{3/2}\Big|_{-R}^{R}\Big) \\
&+2\tan\theta\Big(\frac{1}{8}\big(x\sqrt{\cancel{R^2-x^2}}(2x^2-R^2) + R^4\arctan\frac{x}{\sqrt{\cancel{R^2-x^2}}}\big)\Big)\Big|_{-R}^{R}\Bigg] \\
&= \frac{1}{V}\left[2\tan\theta\frac{1}{8}\Big(R^4\frac{\pi}{2} - -R^4\frac{\pi}{2}\Big)\right] \\
&= \frac{1}{4V}\pi R^4\tan\theta
\end{aligned}$$

$$\begin{aligned}
\bar{y}_\ell^{B*} &= \frac{1}{M}\int\int\int y\rho dV = \frac{1}{M}\left(\frac{M}{V}\right)\int_{-R}^{R}\int_{-\sqrt{R^2-x^2}}^{\sqrt{R^2-x^2}}\int_0^{(R+x)\tan\theta+h_1} ydydzdx \\
&= \frac{1}{V}\frac{1}{2}\int_{-R}^{R}\int_{-\sqrt{R^2-x^2}}^{\sqrt{R^2-x^2}}((R+x)\tan\theta+h_1)^2 dzdx \\
&= \frac{1}{V}\left[\int_{-R}^{R}((R+x)^2\tan^2\theta+2(R+x)h_1\tan\theta+h_1^2)\sqrt{R^2-x^2}dx\right] \\
&= \frac{1}{V}\Bigg[(R^2\tan^2\theta+2Rh_1\tan\theta+h_1^2)\int_{-R}^{R}\sqrt{R^2-x^2}dx \\
&+ (2R\tan^2\theta+2h_1\tan\theta)\int_{-R}^{R}x\sqrt{R^2-x^2}dx+(\tan^2\theta)\int_{-R}^{R}x^2\sqrt{R^2-x^2}dx\Bigg] \\
&= \frac{1}{V}\Bigg[(R\tan\theta+h_1)^2(\frac{1}{2}(x\sqrt{\cancel{R^2-x^2}}+R^2\arctan\frac{x}{\sqrt{\cancel{R^2-x^2}}})\Bigg|_{-R}^{R}) \\
&+(2R\tan^2\theta+2h_1\tan\theta)(-\frac{1}{3}(\cancel{R^2-x^2})^{3/2}\Bigg|_{-R}^{R})+\tan^2\theta\frac{R^4}{8}\arctan\frac{x}{\sqrt{\cancel{R^2-x^2}}}\Bigg|_{-R}^{R}\Bigg] \\
&= \frac{1}{V}\left[(R\tan\theta+h_1)^2\frac{\pi R^2}{2}+\tan^2\theta\frac{\pi R^4}{8}\right] \\
&= \frac{1}{V}\left[(R\tan\theta+\frac{h}{\cos\theta}-2R\tan\theta)^2\frac{\pi R^2}{2}+\tan^2\theta\frac{\pi R^4}{8}\right]
\end{aligned}$$

Case 2: Bottom end partially covered, top end dry

Finding the bounds for h

The bounds for h that define this case depend on the comparison between $h_{top} = L\cos\theta$ and $h_{bottom} = 2R\sin\theta$. This case occurs when $h \in [0, a]$ for $a = \min[L\cos\theta, 2R\sin\theta]$

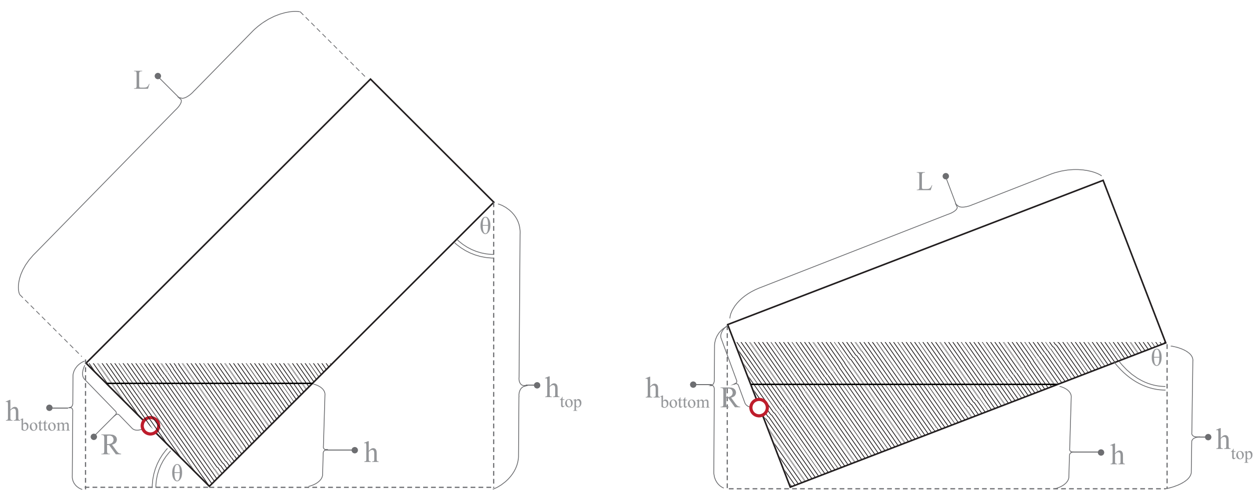

Figure A.4: Diagrams depicting Case 2 for liquid center of mass and volume calculations. (Left) for $h_{top} > h_{bottom}$. (Right) for $h_{top} < h_{bottom}$.

Finding the expression for V

To simplify our expressions, we define the following variables. Let $\alpha = R - \frac{h}{\sin\theta}$ and $\beta = \sqrt{R^2 - \alpha^2}$. To find an expression for V, we evaluate the following integral:

$$\begin{aligned}
V &= \int_{R-\frac{h}{\sin\theta}}^{R} \int_{-\sqrt{R^2-x^2}}^{\sqrt{R^2-x^2}} \int_{0}^{\tan\theta(x-R+\frac{h}{\sin\theta})} dydzdx \\
&= \int_{R-\frac{h}{\sin\theta}}^{R} 2\tan\theta(x - R + \frac{h}{\sin\theta})\sqrt{R^2-x^2}dx \text{ (let } R - \frac{h}{\sin\theta} = \alpha) \\
&= -2\alpha\tan\theta \int_{\alpha}^{R} \sqrt{R^2-x^2}dx + 2\tan\theta \int_{\alpha}^{R} x\sqrt{R^2-x^2}dx \\
&= -2\alpha\tan\theta \left[\frac{1}{2}(x\sqrt{R^2-x^2} + R^2 \arctan\frac{x}{\sqrt{R^2-x^2}}) \Bigg|_{\alpha}^{R} \right] - \frac{2}{3}\tan\theta \left[(R^2-x^2)^{3/2} \Bigg|_{\alpha}^{R} \right] \\
&= -\alpha\tan\theta(\frac{\pi}{2}R^2 - \alpha\sqrt{R^2-\alpha^2} - R^2\arctan\frac{\alpha}{\sqrt{R^2-\alpha^2}}) + \frac{2}{3}\tan\theta(R^2-\alpha^2)^{3/2} \\
&\text{(and letting } \beta = \sqrt{R^2-\alpha^2}) \\
&= \tan\theta(\frac{2\beta^3}{3} - \alpha(\frac{\pi R^2}{2} - \alpha\beta - R^2\arctan\frac{\alpha}{\beta}))
\end{aligned}$$

Finding expressions for the center of mass coordinates

When finding the expressions for the center of mass coordinates, we again use the simplifying variables $\alpha = R - \frac{h}{\sin\theta}$ and $\beta = \sqrt{R^2-\alpha^2}$. We evaluate the following integrals:

$$\begin{aligned}
\bar{x}_\ell^{B*} &= \frac{1}{M}\left(\frac{M}{V}\right)\int_\alpha^R \int_{-\sqrt{R^2-x^2}}^{\sqrt{R^2-x^2}} \int_0^{\tan\theta(x-\alpha)} x dy dz dx \\
&= \frac{1}{V}\left[\int_\alpha^R x\tan\theta(x-\alpha)2\sqrt{R^2-x^2}dx\right] \\
&= \frac{1}{V}\left[-2\alpha\tan\theta\int_\alpha^R x\sqrt{R^2-x^2}dx + 2\tan\theta\int_\alpha^R x^2\sqrt{R^2-x^2}dx\right] \\
&= \frac{1}{V}\left[\frac{2}{3}\alpha\tan\theta(R^2-x^2)^{3/2}\Big|_\alpha^R + \frac{1}{4}\tan\theta(x\sqrt{R^2-x^2}(2x^2-R^2) + R^4\arctan\frac{x}{\sqrt{R^2-x^2}})\Big|_\alpha^R\right] \\
&= \frac{1}{V}\left[-\frac{2}{3}\alpha\tan\theta(R^2-\alpha^2)^{3/2} + \frac{1}{4}\tan\theta(\frac{\pi}{2}R^4 - \alpha\sqrt{R^2-\alpha^2}(2\alpha^2-R^2) - R^4\arctan\frac{\alpha}{\sqrt{R^2-\alpha^2}})\right] \\
&= \frac{1}{V}\tan\theta\left[-\frac{2}{3}\alpha\beta^3 + \frac{1}{4}(\frac{\pi}{2}R^4 - \alpha\beta(2\alpha^2-R^2) - R^4\arctan\frac{\alpha}{\beta})\right]
\end{aligned}$$

$$\begin{aligned}
\bar{y}_\ell^{B*} &= \frac{1}{M}\left(\frac{M}{V}\right)\int_\alpha^R \int_{-\sqrt{R^2-x^2}}^{\sqrt{R^2-x^2}} \int_0^{\tan\theta(x-\alpha)} y dy dz dx \\
&= \frac{1}{V}\int_\alpha^R \tan^2\theta(x-\alpha)^2\sqrt{R^2-x^2}dx \\
&= \frac{1}{V}\int_\alpha^R \tan^2\theta(x^2-2x\alpha+\alpha^2)\sqrt{R^2-x^2}dx \\
&= \frac{1}{V}\left[\tan^2\theta\alpha^2\int_\alpha^R\sqrt{R^2-x^2}dx - 2\tan^2\theta\alpha\int_\alpha^R x\sqrt{R^2-x^2}dx + \tan^2\theta\int_\alpha^R x^2\sqrt{R^2-x^2}dx\right] \\
&= \frac{1}{V}\left[\frac{1}{2}\tan^2\theta\alpha^2(x\sqrt{R^2-x^2} + R^2\arctan\frac{x}{\sqrt{R^2-x^2}})\Big|_\alpha^R + \frac{2}{3}\tan^2\theta\alpha((R^2-x^2)^{3/2})\Big|_\alpha^R\right. \\
&\left.+\frac{1}{8}\tan^2\theta(x\sqrt{R^2-x^2}(2x^2-R^2) + R^4\arctan\frac{x}{\sqrt{R^2-x^2}})\Big|_\alpha^R\right] \\
&= \frac{1}{V}\left[\frac{1}{2}\tan^2\theta\alpha^2(\frac{\pi}{2}R^2 - \alpha\sqrt{R^2-\alpha^2} - R^2\arctan\frac{\alpha}{\sqrt{R^2-\alpha^2}}) - \frac{2}{3}\tan^2\theta\alpha(R^2-\alpha^2)^{3/2}\right. \\
&\left.+\frac{1}{8}\tan^2\theta(\frac{\pi}{2}R^4 - \alpha\sqrt{R^2-\alpha^2}(2\alpha^2-R^2) - R^4\arctan\frac{\alpha}{\sqrt{R^2-\alpha^2}})\right] \\
&= \frac{1}{V}\tan^2\theta\left[\frac{1}{2}\alpha^2(\frac{\pi}{2}R^2 - \alpha\beta - R^2\arctan\frac{\alpha}{\beta}) - \frac{2}{3}\alpha\beta^3 + \frac{1}{8}(\frac{\pi}{2}R^4 - \alpha\beta(2\alpha^2-R^2) - R^4\arctan\frac{\alpha}{\beta})\right]
\end{aligned}$$

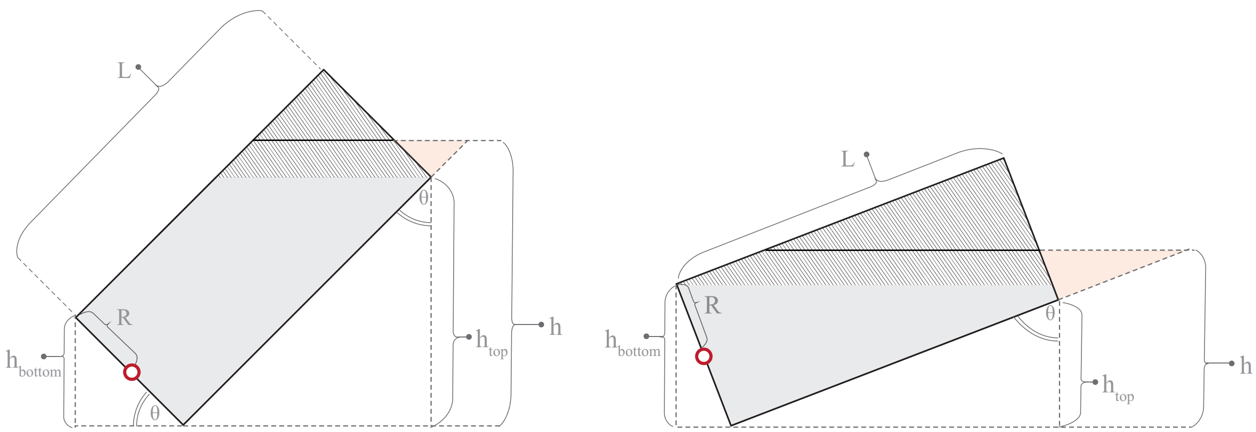

Figure A.5: Diagrams depicting Case 3 for liquid center of mass and volume calculations. (Left) for $h_{top} > h_{bottom}$. (Right) for $h_{top} < h_{bottom}$. Red triangles correspond to volume (case 2) with height $h - L\cos\theta$ to be subtracted from volume (case 1) with height h.

Case 3

Finding the bounds for h

For this specific case, the bounds for h again rely on a comparison between $h_{top} = L\cos\theta$ and $h_{bottom} = 2R\sin\theta$. This case occurs when $h \in [\alpha, L\cos\theta + 2R\sin\theta]$ for $\alpha = \max[L\cos\theta, 2R\sin\theta]$.

Finding the expression for V

The resulting cylindrical wedge of this specific case can be simply calculated as the volumetric difference of a Case 1 wedge with height $h_1 = h$ and a Case 2 wedge with height $h_2 = h - L\cos\theta$. A cross-section of the Case 2 wedge is depicted in red in Figure A.5. If we let $V_i(\cdot)$ denote the volume formula for case (i) as a function of height $(\cdot)$, then the volume of the cylindrical wedge can be calculated as:

$$V_3(h) = V_1(h_1) - V_2(h_2)$$

Finding the expressions for the center of mass coordinates

Additionally, let $\bar{x}^B_{\ell\,i}(\cdot)$ and $\bar{y}^B_{\ell\,i}(\cdot)$ denote the center of mass formulas for case (i) as functions of height $(\cdot)$. Note that, since the centers of mass are calculated in reference to the shifted body frame, with the origin centered at the red dot in Figure A.5, the values for $\bar{y}^B_{\ell\,2}(\cdot)$ will be shifted by the length of the container, L. The center of mass coordinates, with respect to the shifted body frame, are thus calculated as such:

$$\bar{x}^B_{\ell\,3} = \frac{\bar{x}^B_{\ell\,1}(h_1)V_1(h_1) - \bar{x}^B_{\ell\,2}(h_2)V_2(h_2)}{V_1(h_1) - V_2(h_2)}\ ,\ \bar{y}^B_{\ell\,3} = \frac{\bar{y}^B_{\ell\,1}(h_1)V_1(h_1) - (\bar{y}^B_{\ell\,2}(h_2) + L)V_2(h_2)}{V_1(h_1) - V_2(h_2)}$$

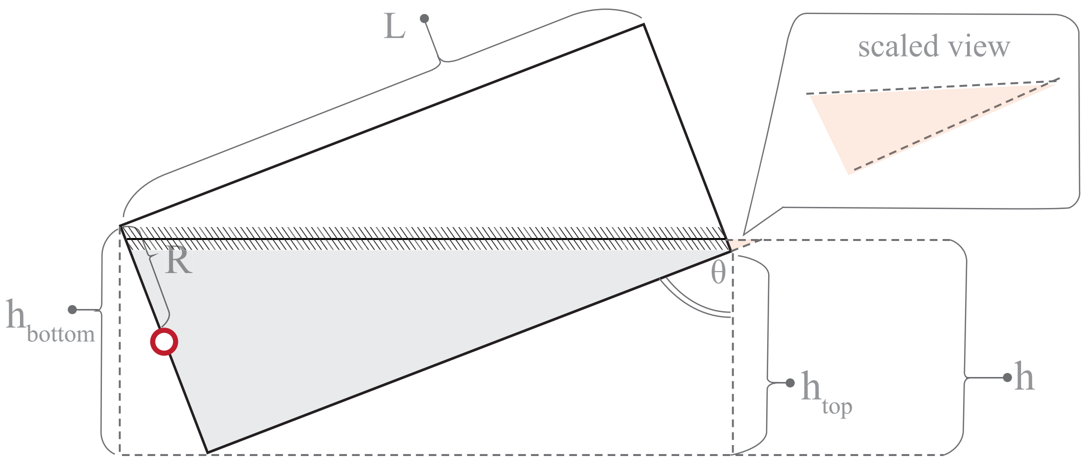

Figure A.6: Diagram depicting Case 4 for liquid center of mass and volume calculations. Red triangle corresponds to volume (case 2) with height $h - L\cos\theta$ to be subtracted from volume (case 2) with height h.

Case 4

Finding the bounds for h

This specific case only occurs when $L\cos\theta < 2R\sin\theta$ and $h \in [L\cos\theta, 2R\sin\theta]$.

Finding the expression for V

The resulting cylindrical wedge of this specific case can be simply calculated as the volumetric difference of a Case 2 wedge with height $h_1 = h$ and a Case 2 wedge with height $h_2 = h - L\cos\theta$. A cross-section of the subtracted Case 2 wedge is depicted in red in Figure A.5. As before, let $V_i(\cdot)$ denote the volume formula for case (i) as a function of height $(\cdot)$. The volume of the cylindrical wedge can be calculated as:

$$V_4(h) = V_2(h_1) - V_2(h_2)$$

Finding the expressions for the center of mass coordinates

As before, let $\bar{x}^B_{\ell\,i}(\cdot)$ and $\bar{y}^B_{\ell\,i}(\cdot)$ denote the center of mass formulas for case (i) as functions of height $(\cdot)$. Note that, since the centers of mass are calculated in reference to the shifted body frame, with the origin centered at the red dot in Figure A.5, the values for $\bar{y}^B_{\ell\,2}(\cdot)$ will be shifted by the length of the container, L. The center of mass coordinates, with respect to the shifted body frame, are thus calculated as such:

$$\bar{x}^B_{\ell\,4} = \frac{\bar{x}^B_{\ell\,2}(h_1)V_2(h_1) - \bar{x}^B_{\ell\,2}(h_2)V_2(h_2)}{V_2(h_1) - V_2(h_2)}\ ,\ \bar{y}^B_{\ell\,4} = \frac{\bar{y}^B_{\ell\,2}(h_1)V_2(h_1) - (\bar{y}^B_{\ell\,2}(h_2) + L)V_2(h_2)}{V_2(h_1) - V_2(h_2)}$$

A.3 Liquid Viscosity

Low-viscous fluids

By inducing sloshing and observing the slosh-induced forces and torques caused by the shifting center of mass of the ever-evolving liquid volume, we can estimate the viscosity of the liquid. A decaying oscillatory wave in either force or torque can be used to estimate this value. As noted in Section 3.3, the authors of [8, 22, 13] define the following empirical model. Let

$$\Delta = \frac{\text{peak amplitude of oscillation}}{\text{peak amplitude of oscillation one cycle later}}$$

be the logarithmic decrement of the decaying oscillation. The damping ratio is then defined by:

$$\gamma = \frac{\Delta}{\sqrt{2\pi^2 + \Delta^2}}$$

For an upright circular cylindrical tank, the damping ratio of the first symmetric mode is given by:

$$\gamma = 0.79\sqrt{\frac{\nu}{R^{3/2}g^{1/2}}}\left[1 + \frac{0.318}{\sinh 1.84h/R}\left(\frac{1-(h/R)}{\cosh 1.84h/R} + 1\right)\right]$$

where ν is the kinematic viscosity of the liquid, R is the radius of the tank, and h is the fill-level of the tank. We want an expression for dynamic viscosity, $\mu = \nu\rho$. Thus, we first rearrange the above equation.

$$\begin{aligned}
\gamma &= 0.79\sqrt{\frac{\nu}{R^{3/2}g^{1/2}}}\left[1 + \frac{0.318}{\sinh 1.84h/R}\left(\frac{1-(h/R)}{\cosh 1.84h/R} + 1\right)\right] \\
\gamma^2 &= \frac{\nu}{R^{3/2}g^{1/2}}0.79^2\left[1 + \frac{0.318}{\sinh 1.84h/R}\left(\frac{1-(h/R)}{\cosh 1.84h/R} + 1\right)\right]^2 \\
\nu &= \gamma^2\sqrt{R^3 g}\left[0.79\left(1 + \frac{0.318}{\sinh 1.84h/R}\left(\frac{1-(h/R)}{\cosh 1.84h/R} + 1\right)\right)\right]^{-2}
\end{aligned}$$

Plugging in the expression for γ and multiplying by ρ, the density of the liquid, we get an expression for the dynamic viscosity μ:

$$\mu = \rho\left(\frac{\Delta}{\sqrt{2\pi^2 + \Delta^2}}\right)^2\sqrt{R^3 g}\left[0.79\left(1 + \frac{0.318}{\sinh 1.84h/R}\left(\frac{1-(h/R)}{\cosh 1.84h/R} + 1\right)\right)\right]^{-2}$$

High-viscous fluids

Instead of observing sloshing dynamics, the viscosity for high-viscous fluids can be estimated by measuring the rise-time of the overdamped torque response induced by rotating the container. Specifically, the approximate time it takes for the liquid to settle from and to the

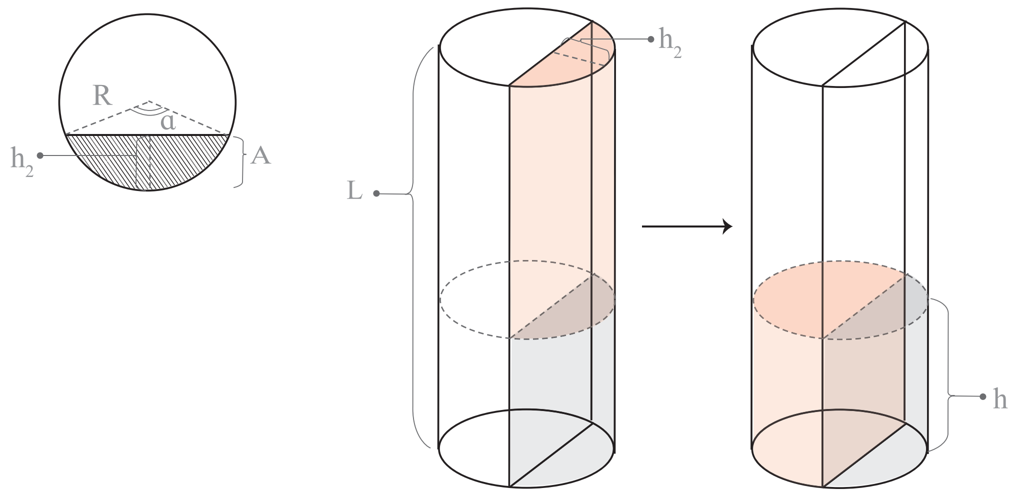

Figure A.7: (Left): Cross-section of liquid flow; (Middle): Highlighted regions (red+grey) are to denote where liquid is present immediately after the rotation of the container. Liquid flows through the cross-sectional area illustrated on the left. (Right): Highlighted regions (red+grey) are to denote where liquid is present after reaching steady state. The red regions are to illustrate the change in location of mass before and after liquid flow.

states illustrated in the middle and right diagrams of Figure A.7 can be used to calculate mass flux, which relates to dynamic viscosity μ.

Mass flux $\mathcal{Q}$ can be approximated by $\frac{\Delta m_\ell}{t_r A}$, where t_r is the measured 10-90% rise time of the damped torque response, Δm_ℓ is the change in mass over that time t_r (corresponding to the red region in Figure A.7, and A is the cross-sectional area through which the mass flows. As shown in Figure A.7, A is the circular segment with height h_2. The formula for this cross-sectional area is given by: $A = \frac{R^2}{2}(\alpha - \sin\alpha)$, where $\alpha = 2\arccos\frac{R-h_2}{R}$. With an estimated volume V, h_2 can be found by searching for the height of the liquid at steady state when the container is tilted by 90 deg. Finally, letting h be the height of the liquid at steady state when the container is tilted by 0 deg, shown on the right in Figure A.7, we can approximate Δm_ℓ by the mass quantity estimated to move during fluid flow induced by the rotation. This corresponds to the mass of the region highlighted in red. We can find Δm_ℓ by multiplying the total mass of the liquid, $_l$, by the ratio of liquid volume that changes location before and after fluid flow. The volume of the red region can be calculated as: $V - Ah$. Thus, $\Delta m_\ell = m_\ell(\frac{V-Ah}{V})$.

For a free surface flow on an inclined plane, mass flux is defined as: $\mathcal{Q} = \frac{\rho g \cos\theta h_2^3}{2\mu}$. Thus, we can rearrange this equation to find μ: $\mu = \frac{\rho g \cos\theta h_2^3}{2\mathcal{Q}}$. Plugging in our approximation of $\mathcal{Q}$ and $\theta = 0$, we get:

$$\mu = \frac{\rho g h_2^3 V t_r A}{2m_\ell(V - Ah)}$$

Bibliography

[1] K. Åström and P. Eykhoff. "System identification—a survey". In: *Automatica* 7.2 (1971), pp. 123–162.

[2] R. Bajcsy. "Active perception". In: *Proceedings of the IEEE* 76.8 (1988), pp. 966–1005.

[3] C. Chen et al. "Learning to identify container contents through tactile vibration signatures". In: *2016 IEEE (SIMPAR)*, pp. 43–48.

[4] S. Chitta et al. "Tactile object class and internal state recognition for mobile manipulation". In: *2010 IEEE (ICRA)*, pp. 2342–2348.

[5] M. Dawson-Haggerty. *Trimesh*. `https://github.com/mikedh/trimesh/blob/master/LICENSE.md`. Accessed: 2019-02-20.

[6] M. Djavareshkian and M Khalili. "Simulation of sloshing with the volume of fluid method". In: *Fluid Dynamics & Materials Processing* 2.4 (2006), pp. 299–308.

[7] C. Do et al. "A probabilistic approach to liquid level detection in cups using an RGB-D camera". In: *2016 IEEE/RSJ (IROS)*, pp. 2075–2080.

[8] F. Dodge et al. *The new" dynamic behavior of liquids in moving containers"*. Southwest Research Inst. San Antonio, TX, 2000.

[9] C. Elbrechter et al. "Discriminating liquids using a robotic kitchen assistant". In: *2015 IEEE/RSJ (IROS)*, pp. 703–708.

[10] J. Feddema et al. "Control for slosh-free motion of an open container". In: *IEEE Control Systems Magazine* 17.1 (1997), pp. 29–36.

[11] P. Güler et al. "What's in the container? Classifying object contents from vision and touch". In: *2014 IEEE/RSJ (IROS)*, pp. 3961–3968.

[12] R. Hess et al. *Liquid gauging using sensor fusion and data fusion*. US Patent 6,157,894. Dec. 2000.

[13] R. Ibrahim. *Liquid sloshing dynamics: theory and applications*. Cambridge University Press, 2005.

[14] D. Katz et al. "Interactive segmentation, tracking, and kinematic modeling of unknown 3d articulated objects". In: *2013 IEEE (ICRA)*, pp. 5003–5010.

[15] D. Katz and O. Brock. “Manipulating articulated objects with interactive perception”. In: *2008 IEEE (ICRA)*, pp. 272–277.

[16] M. Kennedy et al. “Precise dispensing of liquids using visual feedback”. In: *2017 IEEE/RSJ (IROS)*, pp. 1260–1266.

[17] J. Kubricht et al. “Probabilistic Simulation Predicts Human Performance on Viscous Fluid-Pouring Problem.” In: *CogSci*. 2016.

[18] J. Kuehl and J. Capps. *System and method for measuring liquid mass quantity*. US Patent 5,138,559. Aug. 1992.

[19] L. Kunze and M. Beetz. “Envisioning the qualitative effects of robot manipulation actions using simulation-based projections”. In: *Artificial Intelligence* 247 (2017), pp. 352–380.

[20] W. Langlois and M. Deville. *Slow viscous flow*. Vol. 173436. Springer, 1964.

[21] H. Liang et al. “Making Sense of Audio Vibration for Liquid Height Estimation in Robotic Pouring”. In: *arXiv preprint arXiv:1903.00650* (2019).

[22] G Mikishev and N Dorozhkin. “Experimental study of free oscillations of liquid in vessels”. In: *Izv. AN SSSR, OTN, Mekhanika i mashinostroenie* 4 (1961).

[23] B. Mirtich. “Fast and accurate computation of polyhedral mass properties”. In: *Journal of graphics tools* 1.2 (1996), pp. 31–50.

[24] M. Müller et al. “Particle-based fluid simulation for interactive applications”. In: *Proceedings of the 2003 ACM SIGGRAPH/Eurographics (SCA)*, pp. 154–159.

[25] Y. Noda et al. “Flow rate control based on differential flatness in automatic pouring robot”. In: *2011 IEEE (CCA)*. IEEE, pp. 1468–1475.

[26] Z. Pan et al. “Robot motion planning for pouring liquids”. In: *Twenty-Sixth (ICAPS)*. 2016.

[27] Z. Pan and D. Manocha. “Motion planning for fluid manipulation using simplified dynamics”. In: *2016 IEEE/RSJ (IROS)*. IEEE, pp. 4224–4231.

[28] M. Reyhanoglu and J. Hervas. “Point-to-point liquid container transfer via a PPR robot with sloshing suppression”. In: *2012 American Control Conference (ACC)*. IEEE, pp. 5490–5494.

[29] L. Rozo et al. “Force-based robot learning of pouring skills using parametric hidden markov models”. In: *9th (RoMoCo)*. IEEE. 2013, pp. 227–232.

[30] H. Saal et al. “Active sequential learning with tactile feedback”. In: *Proceedings of the Thirteenth (AiStats)*. 2010, pp. 677–684.

[31] C. Schenck and D. Fox. “Perceiving and reasoning about liquids using fully convolutional networks”. In: *IJRR* 37.4-5 (2018), pp. 452–471.

[32] C. Schenck and D. Fox. “Reasoning about liquids via closed-loop simulation”. In: *arXiv preprint arXiv:1703.01656* (2017).

[33] C. Schenck and D. Fox. “Visual closed-loop control for pouring liquids”. In: *2017 IEEE (ICRA)*. IEEE, pp. 2629–2636.

[34] D. Takagi and H. Huppert. “Pouring viscous fluid out of a tipped container in minimal time”. In: *Physical Review E* 84.3 (2011), p. 035303.

[35] A. Yamaguchi and C. Atkeson. “Stereo vision of liquid and particle flow for robot pouring”. In: *2016 IEEE-RAS 16th (Humanoids)*. IEEE, pp. 1173–1180.

[36] W. Yang et al. “Viscous liquid sloshing damping in cylindrical container using a volume of fluid method”. In: *Science in China Series E: Technological Sciences* 52.6 (2009), pp. 1484–1492.

[37] C. Zhang and T. Chen. “Efficient feature extraction for 2D/3D objects in mesh representation”. In: *Proceedings 2001 International Conference on Image Processing*. Vol. 3. IEEE, pp. 935–938.